The 4 $^3\Sigma^+$ state of NaK: Potential energy curve and hyperfine structure

P. Burns, L. Sibbach-Morgus, and A. D. Wilkins
Department of Physics, Lehigh University, Bethlehem, Pennsylvania 18015

F. Halpern
*Department of Physics, Lehigh University, Bethlehem, Pennsylvania 18015 and School of Theoretical
& Applied Science, Ramapo College of New Jersey, Mahwah, New Jersey 07430*

L. Clarke
*Department of Physics, Lehigh University, Bethlehem, Pennsylvania 18015 and Department of Physics,
Amherst College, Amherst, Massachusetts 01002*

R. D. Miles
Department of Physics, Lehigh University, Bethlehem, Pennsylvania 18015

Li Li
*Department of Physics and Key Lab of Atomic and Molecular Nanosciences, Tsinghua University,
Beijing 100084, China*

A. P. Hickman and J. Huennekens
Department of Physics, Lehigh University, Bethlehem, Pennsylvania 18015

High-resolution spectra, including hyperfine structure, have been observed for numerous vibrational-rotational levels (v,N) of the 4 $^3\Sigma^+$ Rydberg state of the NaK molecule. The data have been used to construct a Rydberg–Klein–Rees potential curve, and this molecular potential has been further refined using the inverse perturbation approximation method. Bound-free emission from the 4 $^3\Sigma^+$ electronic state to the repulsive $a(1)\,^3\Sigma^+$ state has also been measured and used to determine both the absolute vibrational numbering and the transition dipole moment function $M(R)$. The experimentally derived potential curve and $M(R)$ are compared with recent theoretical calculations of Magnier *et al.*; the agreement is very good. Each of the levels (v,N) is typically split into three sets of sublevels by the Fermi contact interaction $b\mathbf{I\cdot S}$. Further splitting (of order 0.004 cm^{-1}) has been attributed to the spin-rotation interaction $\gamma\mathbf{N\cdot S}$. The patterns observed exhibit a clear transition from Hund's case $b_{\beta S}$ for small N toward Hund's case $b_{\beta J}$ for large N. The data can be fitted very well using a theoretical model based on setting up and diagonalizing a 12×12 Hamiltonian matrix with two adjustable parameters (b and γ). The values of b that fit the data best are $\sim(0.99 \pm 0.04)\times10^{-2}$ cm^{-1}, with a weak dependence on v. The best fit values of γ are in the range $1-6\times10^{-4}$ cm^{-1} and depend strongly on v. The values of γ appear to exhibit anomalous structure for (v,N) levels perturbed by nearby levels of the 3 $^3\Pi$ state. © *2003 American Institute of Physics.* [DOI: 10.1063/1.1590638]

I. INTRODUCTION

In our laboratory we are carrying out a program of high-resolution spectroscopic studies of the fine and hyperfine structure of excited triplet states of NaK. Sodium–potassium mixtures are of current interest for mixed-species atom traps, and the NaK high-lying triplet states are of particular interest for the understanding of future sodium–potassium photoassociation spectra. Recently we published an initial investigation[1] of the 1 $^3\Delta$ state of NaK. In the present paper we extend our work to the 4 $^3\Sigma^+$ state. One of the most interesting features of this work is the demonstration that different electronic states of NaK exhibit quite different behavior. Different electronic states, and even different rotational levels within the same electronic state, often exhibit strikingly different hyperfine structure. The analysis of this behavior will provide important information about fundamental electronic and magnetic interactions in molecules.

As in our previous work,[1] we use the technique of "perturbation-facilitated, optical–optical double resonance" (PFOODR) (Refs. 2–29) to probe excited triplet states. This technique involves two-step excitation from the singlet ground state to a highly excited triplet state through specific intermediate-state rovibrational "window" levels that display both singlet and triplet character due to perturbations. When one uses narrow-band continuous-wave (cw) lasers (as we do), this technique is also capable of very high resolution since it is inherently Doppler free. Previous studies using this method have investigated the hyperfine structure of many triplet states of Na$_2$ (Refs. 6–12 and 30–34), a few triplet states of Li$_2$ (Refs. 6, 14, 15, 29, and 35), and also triplet states of NaRb (Refs. 36 and 37) and NaK (Refs. 3, 26–28, and 38–40).

We have measured the average energies of a total of 107 vibrational-rotational levels (v,N) with $0\leq v\leq33$ and $14\leq N\leq46$. The potential curve of the 4 $^3\Sigma^+$ state is not com-

pletely smooth; calculations by Magnier *et al.*[41,42] indicate that it should exhibit a slight shelf. Our results indicate that a traditional Dunham expansion of the (v,N) level energies is unsatisfactory, so we developed an alternative expansion and used it to construct the Rydberg–Klein–Rees (RKR) potential curve. This RKR curve was then refined using the inverse perturbation approximation (IPA) method.[43] Both the RKR and IPA potentials exhibit a shelf that is slightly more pronounced than the one predicted by the calculations.

The $4\,^3\Sigma^+$ state exhibits novel hyperfine structure since as a Σ state its first-order spin–orbit interaction is zero. This case is quite different from the situation observed in our previous study[1] of the $1\,^3\Delta$ state, where for each level (v,N) a large spin–orbit interaction leads to a coarse structure, and then the Fermi contact interaction $b\mathbf{I}\cdot\mathbf{S}$ leads to a finer splitting. For the $4\,^3\Sigma^+$ state, the Fermi contact interaction leads to the coarse structure, and a still finer structure has been observed, which we attribute to the spin-rotation interaction $\gamma\mathbf{N}\cdot\mathbf{S}$. The angular momentum coupling approximately follows Hund's case $b_{\beta S}$, although systematic deviations from this limit in the direction of case $b_{\beta J}$ are clearly seen as N (nuclear rotation) increases. By numerically diagonalizing a model Hamiltonian, we are able to reproduce the observed energy levels for intermediate coupling cases with high accuracy. We achieve a satisfactory fit to the observed hyperfine energies of each rovibrational level with the adjustable parameters b and γ. The value of b depends weakly on v, and γ depends strongly on v.

This paper is organized as follows: Section II describes the details of the experiment and the data obtained. Section III describes the analysis and interpretation of the data. The discussion includes the spectroscopic parameters for the vibrational and rotational energy levels, the RKR and IPA potentials for the $4\,^3\Sigma^+$ state, the general features of the hyperfine structure, and the methodology we have developed to model that structure. Section IV contains concluding remarks.

II. EXPERIMENT

The experimental setup is the same as that described in Ref. 1 and is shown in Fig. 1 of that reference. Briefly, a mixture of sodium and potassium is heated in a four-arm cross heat-pipe oven.[44] The oven temperature is maintained in the range $361-395\,°C$. The densities of the various atomic and molecular species (at $T\sim380\,°C$) are $\sim3.6\times10^{16}$ cm^{-3} (atomic potassium), 3.2×10^{15} cm^{-3} (atomic sodium), 2.9×10^{14} cm^{-3} (K$_2$), 5.8×10^{13} cm^{-3} (Na$_2$), and 1.6×10^{14} cm^{-3} (NaK).[45,46] Argon gas at a pressure of 1–3 Torr in the oven is used to keep the hot alkali vapor away from the oven windows.

The basic idea of the PFOODR experiment is depicted schematically in Fig. 1. A single-mode cw dye laser (Coherent model 699-29, ~300 mW output power in the 720–760 nm range using LD700 dye when pumped by a 5-W krypton ion laser) is used as the pump laser to excite NaK molecules on various $b(1)\,^3\Pi(v_b,J)\sim A(2)\,^1\Sigma^+(v_A,J)$ $\leftarrow X(1)\,^1\Sigma^+(v_X,J\pm1)$ transitions, where the upper level is a mixed singlet-triplet "window" level. A single-mode cw
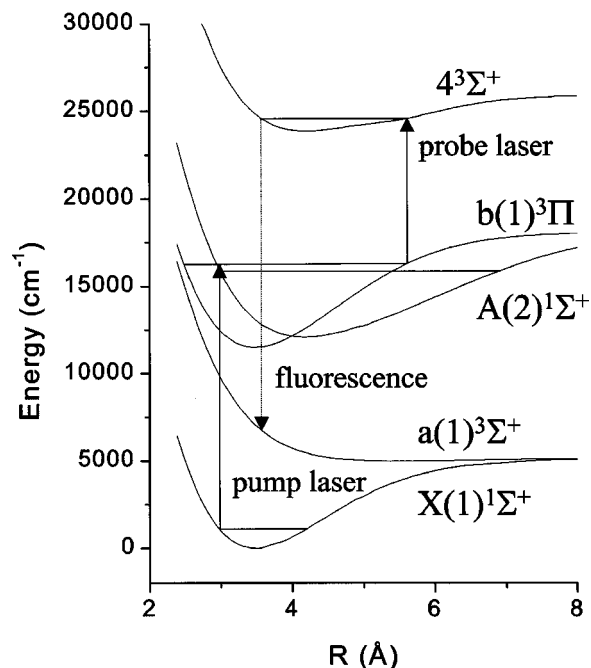

FIG. 1. Schematic diagram showing NaK molecular potentials and the PFOODR pumping scheme used in this experiment.

Ti:sapphire laser (Coherent model 899-29, 500–600 mW output power in the range 700–900 nm when pumped by a 10-W argon ion laser) is used as the probe laser to excite the NaK molecules further to various levels of the $4\,^3\Sigma^+$ state, i.e., $4\,^3\Sigma^+(v_\Sigma,N=J\pm1)\leftarrow b(1)\,^3\Pi(v_b,J)$ $\sim A(2)\,^1\Sigma^+(v_A,J)$. The pump and probe beams are focused with 100 and 200 cm focal-length lenses, respectively, and the beams counterpropagate through the oven. In the later stages of the experiment we found we could improve the signal-to-noise ratio by adding 67 and 44.4 cm focal-length lenses to the pump and probe beam paths, respectively.

Several detectors are used to collect laser-induced fluorescence emitted in a direction perpendicular to the axis of the laser beams. A freestanding photomultiplier tube (PMT) (Hamamatsu R406), equipped with a 700–1000 nm bandpass filter, is used to monitor total $A(2)\,^1\Sigma^+(v_A,J)$ $\rightarrow X(1)\,^1\Sigma^+(v_X,J\pm1)$ fluorescence as the pump laser frequency is scanned. Once a particular $b(1)\,^3\Pi(v_b,J)$ $\sim A(2)\,^1\Sigma^+(v_A,J)$ window level is located, the pump laser frequency is fixed to line center of the appropriate transition. A second freestanding PMT (Hamamatsu R928) is equipped with either a set of three 364–539 nm bandpass filters (Oriel model 51710) with a 465 nm transmission peak or with a 400–550 nm bandpass filter (SCOG model QB23) in combination with a 625 nm shortpass filter (Reynard model 935). This detector is used to monitor bound-free NaK $4\,^3\Sigma^+\rightarrow a(1)\,^3\Sigma^+$ fluorescence as the probe laser frequency is tuned through various $4\,^3\Sigma^+(v_\Sigma,N=J\pm1)$ $\leftarrow b(1)\,^3\Pi(v_b,J)\sim A(2)\,^1\Sigma^+(v_A,J)$ transitions. Doppler-free transitions to levels of the $4\,^3\Sigma^+$ state can easily be distinguished from transitions to other triplet electronic states in the same probe laser frequency range by their distinctive signature pattern (see Fig. 2). The pump laser is mechanically chopped and lock-in detection is employed. Resolved
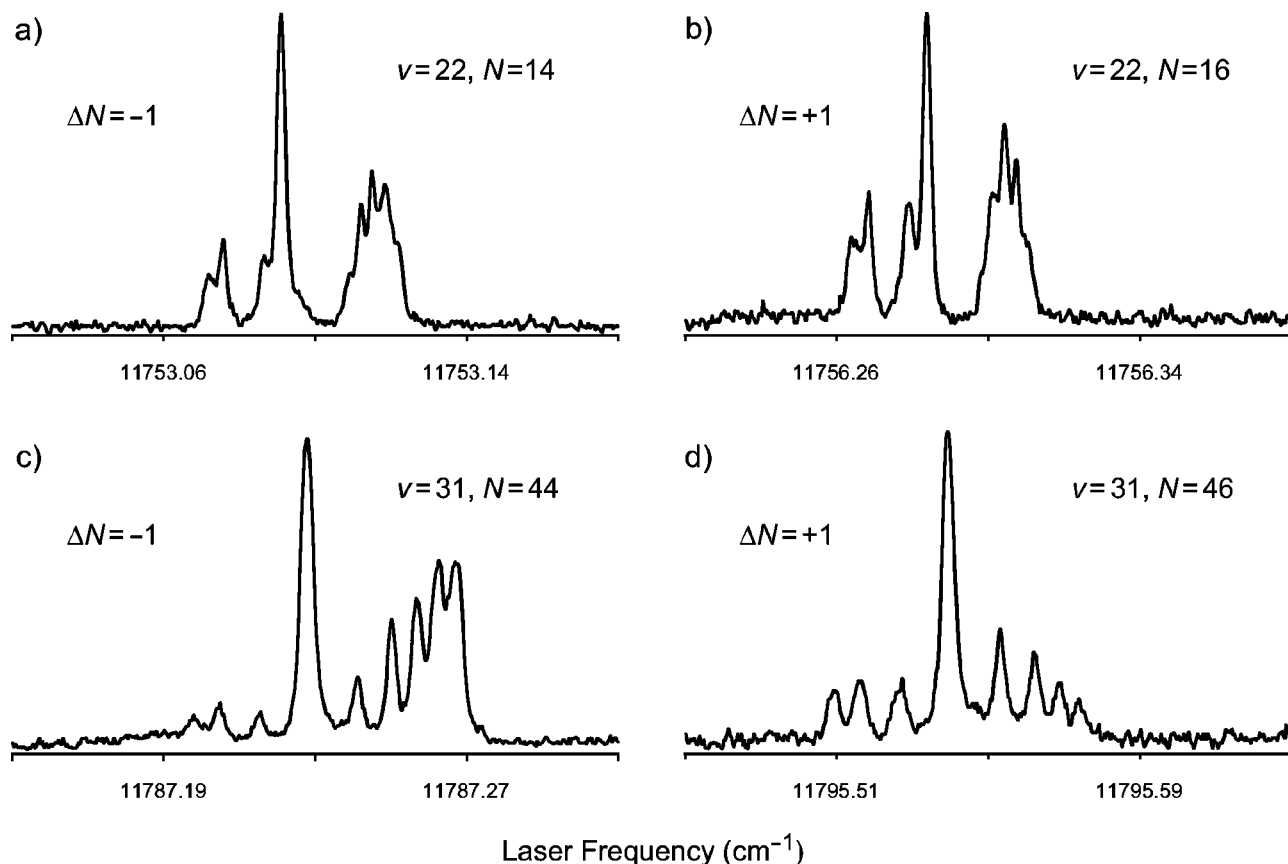
J. Chem. Phys., Vol. 119, No. 9, 1 September 2003

The 4 $^3\Sigma^+$ state of NaK 4745

FIG. 2. 4 $^3\Sigma^+$ hyperfine structure for different N values. P branch transitions ($\Delta N = -1$) are on the left, and R branch transitions ($\Delta N = +1$) are on the right.

fluorescence scans can also be recorded with a monochromator–PMT system. In the present experiment, resolved bound-free $4\,^3\Sigma^+ \rightarrow a(1)\,^3\Sigma^+$ fluorescence was recorded with the pump and probe lasers fixed to a particular $4\,^3\Sigma^+(v_\Sigma, N = J \pm 1) \leftarrow b(1)\,^3\Pi(v_b, J) \sim A(2)\,^1\Sigma^+(v_A, J) \leftarrow X(1)\,^1\Sigma^+(v_X, J \pm 1)$ double-resonance transition. These scans were used to determine the absolute vibrational numbering of the $4\,^3\Sigma^+(v_\Sigma)$ levels as described below. The detection efficiency of the monochromator–PMT system as a function of wavelength was determined using a calibrated tungsten-halogen white light source.[47]

The wavemeter of the pump laser was calibrated by comparing frequencies of I_2 laser-induced fluorescence lines to those listed in the iodine atlas.[48] The probe laser wavemeter was calibrated using optogalvanic signals from neon transitions in a hollow cathode lamp. Absolute energies of $4\,^3\Sigma^+(v_\Sigma, N)$ levels are considered to be accurate to ~ 0.02 cm^{-1}. However, splittings between hyperfine and spin-rotation components are determined to much higher accuracy, typically 0.001 cm^{-1} (30 MHz).

III. ANALYSIS AND RESULTS

A. Rotational level structure and vibrational numbering

Transitions to the NaK $4\,^3\Sigma^+$ state are easily distinguished from those to other nearby triplet states because they display the characteristic signature patterns shown in Fig. 2. These rotational line patterns look quite similar to those of

the ^{6}Li^{7}Li $3\,^3\Sigma_g^+$ state[35] and are formed by a combination of hyperfine structure (Fermi contact interaction) and the spin-rotation interaction. They are also very different from the line shapes associated with the $1\,^3\Delta$ state[1] and the $3\,^3\Pi$ state.[49] A discussion of this structure is given in Secs. III E and III F below. The $+/-$ parity of an intermediate state window level $b(1)\,^3\Pi(v_b, J) \sim A(2)\,^1\Sigma^+(v_A, J)$ is given by $(-1)^J$. Similarly, the parity of a $4\,^3\Sigma^+(v, N)$ level is given by $(-1)^N$. Due to the dipole selection rules, $+ \leftrightarrow -$, $+ \not\leftrightarrow +$, $- \not\leftrightarrow -$ transitions are observed from a given intermediate window level $b(1)\,^3\Pi(v_b, J) \sim A(2)\,^1\Sigma^+(v_A, J)$ to only two $4\,^3\Sigma^+$ rotational levels, characterized by $N = J \pm 1$ (R and P lines) for each vibrational level v_Σ.

The intensities for P line pumping ($\Delta N \equiv N_{\text{upper}} - N_{\text{lower}} = -1$) shown in Fig. 2(c) build at the high-frequency end of the hyperfine multiplet line shape. Conversely, the R line ($\Delta N = +1$) intensities shown in Fig. 2(d) trail off at the high-frequency end. This behavior can be qualitatively understood by considering selection rules, as shown in Fig. 3. The lines drawn correspond to the possible transitions that satisfy the selection rule $\Delta F = 0, \pm 1$. Because of the details of our two-laser pumping scheme,[1] every transition that reaches a particular upper state contributes to the peak corresponding to that upper state. The initial window level does not matter. Thus, in a simple statistical model, the intensity of each observed peak is proportional to the number of allowed transitions reaching the corresponding upper hyperfine level. For P lines, shown on the left, no transition is
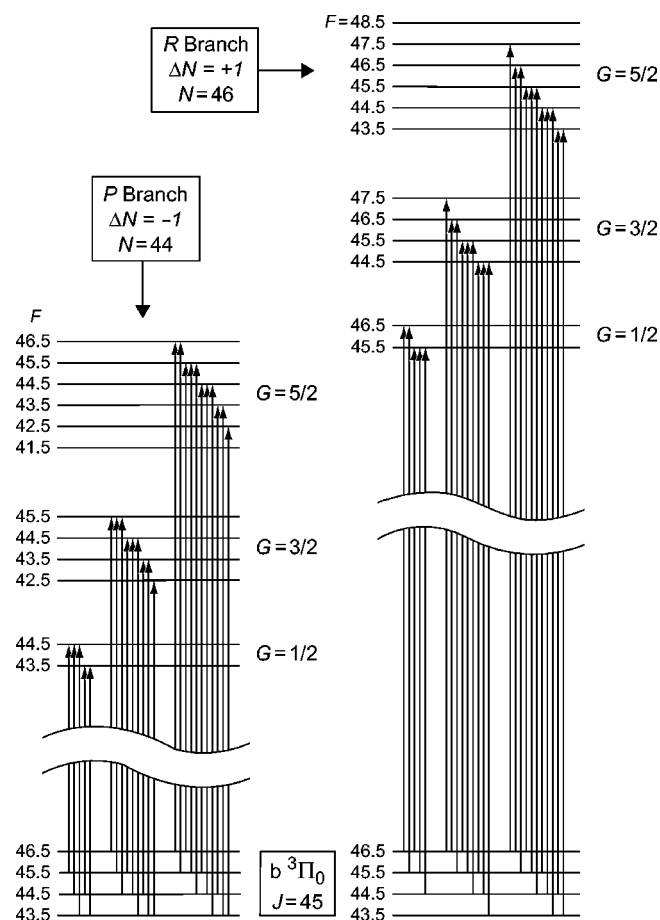
FIG. 3. $4\,^3\Sigma^+$ state rotational line structure and selection rules.

possible from a window level to the lowest energy level of the $G=\frac{5}{2}$ multiplet; only one transition is possible to the next highest, two transitions to the next, and so forth. The R lines on the right exhibit the opposite behavior: no transition is possible from a window level to the highest energy level of the $G=\frac{5}{2}$ multiplet, and there is a gradual increase in the number of transitions possible as the frequency decreases. These arguments provide a qualitative explanation of the contrasting behaviors of the P and R branch scans shown in Figs. 2(c) and 2(d). They also demonstrate that the spin-rotation constant γ is positive (see below).

Five previously known[1,50,51] intermediate state window levels (listed in Table I) were used to record the present spectra. In all, 114 transitions were recorded, representing

TABLE I. Vibrational and rotational quantum numbers for the window levels originally observed in Refs. 1, 50, and 51. The window levels are described by the designation $b(1)\,^3\Pi(v_b,J)\sim A(2)\,^1\Sigma^+(v_A,J)$. In each case, either the mostly singlet or the mostly triplet component can be used as the intermediate level in the PFOODR pumping scheme.

v_b	J	v_A
15	15	15
17	26	18
15	27	15
12	38	11
18	45	20

$4\,^3\Sigma^+$ vibrational levels ranging from 0 to 33 and rotational levels $N=14, 16, 25, 26, 27, 28, 37, 39, 44,$ and 46 (107 total $4\,^3\Sigma^+$ levels). The observed transitions are available electronically.[52]

The absolute vibrational numbering was determined from the spectrally resolved $4\,^3\Sigma^+\rightarrow a(1)\,^3\Sigma^+$ bound-free fluorescence recorded with the pump and probe laser frequencies fixed to populate a particular upper state level $4\,^3\Sigma^+(v_\Sigma,N)$. Examples of these spectra are shown in Fig. 4(a) for $v_\Sigma=0, 1, 2, 3, 4,$ and 8 (with $N=37$). According to the classical Franck–Condon principle, the oscillations in the continuous spectrum directly reflect the oscillations in the upper bound-state radial probability distribution (radial wave function squared).[50] Because the $4\,^3\Sigma^+ - a(1)\,^3\Sigma^+$ difference potential is a monotonic function over the region of internuclear separation spanned by the upper bound-state wave function, the number of nodes in the spectrum gives a direct measure of the vibrational numbering of the upper state level. Figure 4(b) shows quantum mechanical simulations[53] of the same $4\,^3\Sigma^+(v,N=37)\rightarrow a(1)\,^3\Sigma^+$ emission based upon the experimental IPA $4\,^3\Sigma^+$ potential determined here, the composite experimental $a(1)\,^3\Sigma^+$ potential of Refs. 28 and 54, and the theoretical dipole moment function of Magnier *et al.*[42] These results are discussed further in Sec. III D.

B. The $4\,^3\Sigma^+$ RKR potential

The $4\,^3\Sigma^+$ state is a "shelf" state due to interactions among several $^3\Sigma^+$ states.[41,42] The shelf manifests itself by a kink in the plot of the vibrational level spacing (ΔG_v) versus vibrational level v. Figure 5 shows such a plot created using the theoretical $4\,^3\Sigma^+$ state potential of Magnier *et al.*[41,42] (solid circles). Figure 6 shows a similar plot of the dependence of the rotational constant B_v on vibrational quantum number v.

It is clear from the plots shown in Figs. 5 and 6 that a Dunham expansion is unlikely to produce a good fit to the data, and this was indeed found to be the case. Instead, preliminary values of T_v, B_v, and D_v were determined for each $4\,^3\Sigma^+$ vibrational level for which at least three different N's were available by fitting to the quadratic function $E(v,N) = T_v + B_v x - D_v x^2$, where $x = N(N+1)$. The values of D_v were fairly constant, and the average was $\bar{D} = 2.169 \times 10^{-7}$ cm^{-1}. Then we fixed D_v at this value for all v's and determined the final values of T_v and B_v for each investigated vibrational level using the function $E(v,N) = T_v + B_v x - \bar{D}x^2$. The results, which are listed in Table II, reproduce the experimental energies with a standard deviation of 0.019 cm^{-1}. Experimental values of $\Delta G_v = T_v - T_{v-1}$ and B_v obtained in this work are also plotted in Figs. 5 and 6. Comparison of the experimental and theoretical ΔG_v values in Fig. 5 indicates that the change of slope in the potential curve at the shelf is more pronounced than theory predicts.

We found we could accurately fit T_v and B_v using a quadratic polynomial in $(v+\frac{1}{2})$ as a first approximation and then adding a Fourier series to represent the residual oscillations. The explicit forms of the fitting functions we used are
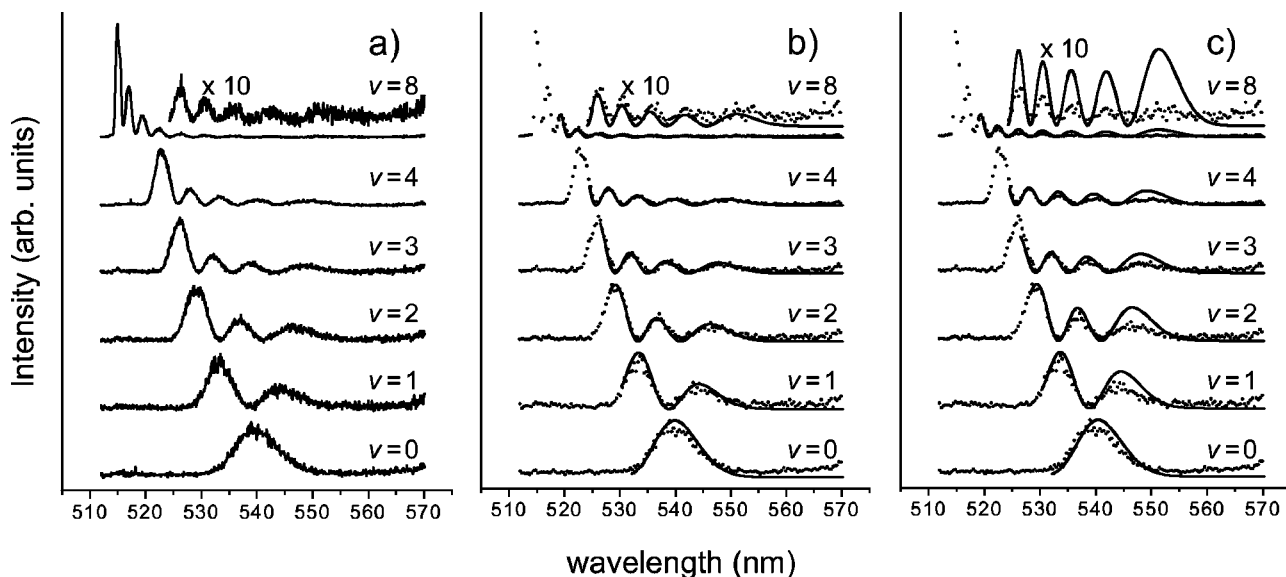
FIG. 4. Measured and simulated $4\,^3\Sigma^+(v,N=37)\rightarrow a(1)\,^3\Sigma^+$ bound-free fluorescence spectra. Panel (a) shows the experimental spectra (intensity per unit wavelength interval) corrected for the relative detection system efficiency vs wavelength. Panel (b) shows spectra simulated using the experimental IPA potential determined in the present work and the theoretical transition dipole moment function of Magnier et al. (Ref. 42) (solid lines) plus, for comparison, every fifth data point from panel (a). Panel (c) shows spectra simulated using a dipole moment function that is constant with internuclear separation R. In (b) and (c) the theoretical spectra were scaled to the experimental spectra at the shortest wavelength peak for $v=0$, 1 and 2, at the second peak for $v=3$ and 4, and at the third peak for $v=8$.

$$T_v = C_1 + C_2 y + C_3 y^2 + \sum_{n=1}^{10} C_{n+4} \cos(nC_4 y) \qquad (1)$$

and

$$B_v = C_1' + C_2' y + C_3' y^2 + \sum_{n=1}^{10} C_{n+4}' \cos(nC_4' y), \qquad (2)$$

where $y = v + \frac{1}{2}$. The constants C_n and C_n' are listed in Table III. The T_v and B_v functions in Eqs. (1) and (2), combined with the fixed value $\bar{D} = 2.169 \times 10^{-7}$ cm^{-1}, reproduce the experimental energies with a standard deviation of

0.41 cm^{-1}. Conventional spectroscopic constants T_e, ω_e, $\omega_e x_e$, and B_e, derived from the fitting constants, are also listed in Table III.

Finally, we modified LeRoy's RKR1 program[55] slightly so that it would accept these functions rather than Dunham coefficients and would use them to determine an RKR potential for the $4\,^3\Sigma^+$ state. The RKR turning points are listed in Table 2 of the accompanying EPAPS file.[52] The program LEVEL 7.4 (Ref. 56) was used to calculate energies of $4\,^3\Sigma^+(v,N)$ levels from the RKR potential. The RKR points $R_{\min}(v)$ and $R_{\max}(v)$ were truncated for $v > 30$. LEVEL extrapolated the potential points to smaller values of R using an
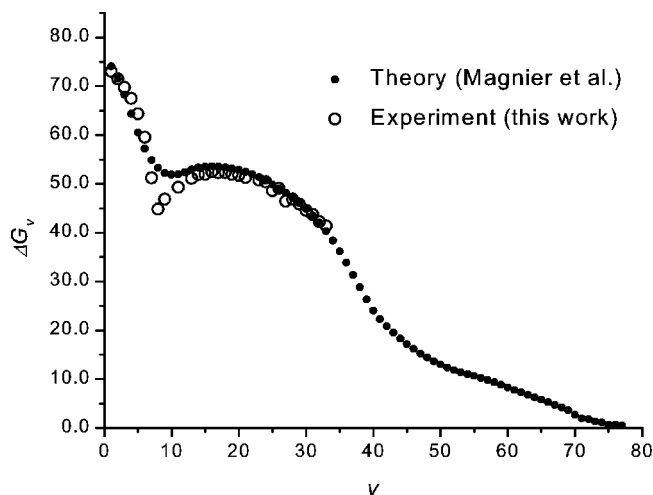

FIG. 5. ΔG_v vs v for $4\,^3\Sigma^+$: theory and experiment. The points labeled "theory" were calculated by us using the theoretical $4\,^3\Sigma^+$ potential curve of Magnier et al. (Refs. 41 and 42).

FIG. 6. B_v vs v for $4\,^3\Sigma^+$: theory and experiment. The points labeled "theory" were calculated by us using the theoretical $4\,^3\Sigma^+$ potential curve of Magnier et al. (Refs. 41 and 42).
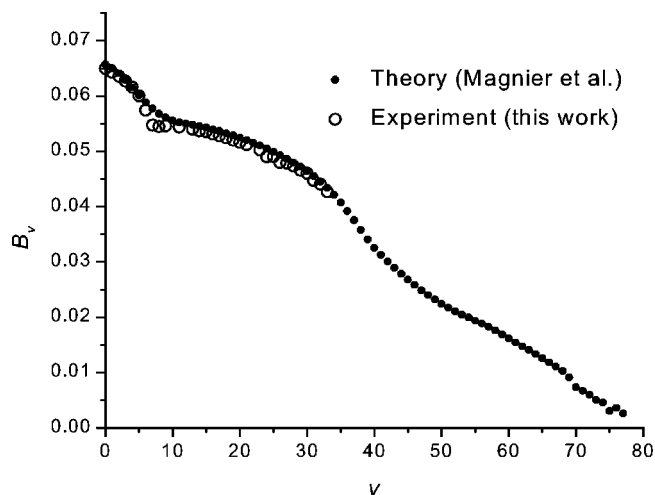
TABLE II. Measured values of T_v, ΔG_v, and B_v for the NaK 4 $^3\Sigma^+$ state. In the fits, D_v was fixed at the value $\bar{D}=2.169\times10^{-7}$ cm^{-1} for all v. Uncertainties in the least significant digits are given in parentheses. Uncertainties are only reported for vibrational levels where three or more rotational levels were recorded.

v	T_v (cm^{-1})	ΔG_v (cm^{-1})	B_v (cm^{-1})
0	23979.382		0.06496
1	24052.450	73.069	0.06429
2	24123.973(9)	71.522	0.06356(1)
3	24193.724	69.752	0.06270
4	24261.235(32)	67.511	0.06160(2)
5	24325.597	64.361	0.06005
6	24385.158(7)	59.562	0.05746(1)
7	24436.390	51.232	0.05473
8	24481.217(22)	44.826	0.05447(1)
9	24528.081	46.864	0.05462
10			
11	24626.715	49.317	0.05439
12			
13	24728.974	51.130	0.05399
14	24780.921	51.947	0.05367
15	24832.873	51.952	0.05355
16	24885.359(8)	52.486	0.05314(1)
17	24937.676(9)	52.317	0.05282(1)
18	24989.973(2)	52.297	0.05243(1)
19	25041.938(8)	51.966	0.05204(1)
20	25093.728(11)	51.789	0.05164(1)
21	25145.054(2)	51.326	0.05120(1)
22			
23	25246.651(16)	50.798	0.05028(1)
24	25297.070	50.420	0.04901
25	25345.684	48.614	0.04906
26	25394.804(9)	49.120	0.04796(1)
27	25441.258(5)	46.454	0.04786(1)
28	25488.130(5)	46.872	0.04734(1)
29	25534.020(25)	45.890	0.04661(1)
30	25578.618(3)	44.598	0.04605(1)
31	25622.333(29)	43.715	0.04473(3)
32	25664.576(2)	42.243	0.04406(1)
33	25705.989(4)	41.414	0.04271(1)

exponential function and to larger values of R using an inverse power law. This procedure improved the agreement between the experimental and calculated energies for $30 \leqslant v \leqslant 33$. The calculated energies match the experimental energies for all measured levels ($v=0-33$) with a standard deviation of 0.55 cm^{-1}.

C. IPA potential

The inverse perturbation approximation (IPA) method[43] can be used to find a potential $V(R)$ whose calculated rovibrational energy levels $E_{\text{calc}}(v,N)$ match experimentally measured energies as closely as possible. The methodology has been documented;[43] the essential feature is that one starts with an approximate "reference" potential $V_0(R)$ whose energies roughly match the experimental values and seeks to find a potential

$$V(R)=V_0(R)+\delta V(R) \tag{3}$$

that matches the data better. The method is based on varying the values of $\delta V(R)$ at a set of P points $R_1,R_2,\ldots,R_P$ in order to achieve the best agreement between experiment and calculation. Values of $\delta V(R)$ at intermediate points are obtained by cubic spline. The method normally must be iterated. One uses the $V(R)$ found in one cycle as the "reference" potential for the next cycle.

The calculations reported here were performed using a modified version of the publicly available code.[43] We simplified the input files required, and we adapted subroutines from the program LEVEL (Ref. 56) to calculate the rovibrational energy levels of the reference potential. Using LEVEL has the advantage that initial guesses for the energy levels are not required.

Because the IPA method adjusts the values of the potential on a grid of points, it can introduce unphysical structure ("wiggles") into the result. To minimize this effect in the present case, we decided first to smooth the RKR potential presented above, since the RKR curve already showed some
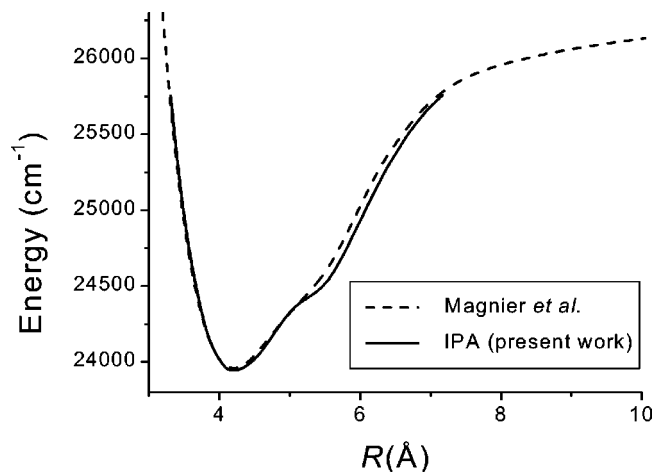
TABLE III. Spectroscopic constants and fitting constants for T_v and B_v for the NaK 4 $^3\Sigma^+$ state. The fitting constants are defined in the text in Eqs. (1) and (2). The large numbers of digits reported in the fitting constants, which are more than are statistically significant, are required to reproduce the experimental energies to within the accuracy quoted in the text.

Spectroscopic constants (cm^{-1})		Fitting constants (cm^{-1})			
		Vibrational		Rotational	
T_e	23940.45 ± 0.23	C_1	23795.4733 ± 18.0	C_1'	$8.6560\text{E}-02\pm9.0\text{E}-03$
ω_e	78.94 ± 0.03	C_2	78.94285 ± 1.9	C_2'	$-2.5334\text{E}-03\pm8.8\text{E}-04$
$\omega_e x_e$	2.8694 ± 0.0009	C_3	-0.579504 ± 0.037	C_3'	$2.2663\text{E}-05\pm1.5\text{E}-05$
B_e	0.0662 ± 0.0001	$C_4{}^{\text{a}}$	0.111 ± 0.007	$C_4'{}^{\text{a}}$	$9.7310\text{E}-02\pm5.0\text{E}-03$
		C_5	115.3688 ± 10.9	C_5'	$-1.6491\text{E}-02\pm5.4\text{E}-03$
		C_6	32.1167 ± 4.6	C_6'	$-1.402\text{E}-03\pm1.4\text{E}-03$
		C_7	1.8456 ± 2.3	C_7'	$-2.84\text{E}-04\pm6.2\text{E}-04$
		C_8	-3.6579 ± 0.83	C_8'	$2.73\text{E}-04\pm3.9\text{E}-04$
		C_9	-3.7362 ± 0.56	C_9'	$-2.92\text{E}-04\pm3.2\text{E}-04$
		C_{10}	-1.2245 ± 1.0	C_{10}'	$-3.78\text{E}-04\pm1.9\text{E}-04$
		C_{11}	0.7121 ± 0.64	C_{11}'	$-6.42\text{E}-04\pm2.3\text{E}-04$
		C_{12}	1.5045 ± 0.44	C_{12}'	$-5.99\text{E}-04\pm1.4\text{E}-04$
		C_{13}	1.5258 ± 0.29	C_{13}'	$-3.54\text{E}-04\pm1.1\text{E}-04$
		C_{14}	0.5250 ± 0.58	C_{14}'	$-2.37\text{E}-04\pm1.3\text{E}-04$

$^{\text{a}}C_4$ and C_4' are dimensionless.

FIG. 7. Comparison of the IPA potential for the $4\,^3\Sigma^+$ state of NaK (solid curve) with the theoretical calculation of Magnier et al. (dashed curve) (Refs. 41 and 42). The RKR curve is not plotted because on the scale of this figure, it would be difficult to see the difference between the IPA and RKR curves. At all R values, the difference between the IPA and RKR curves is less than 30 cm^{-1}.
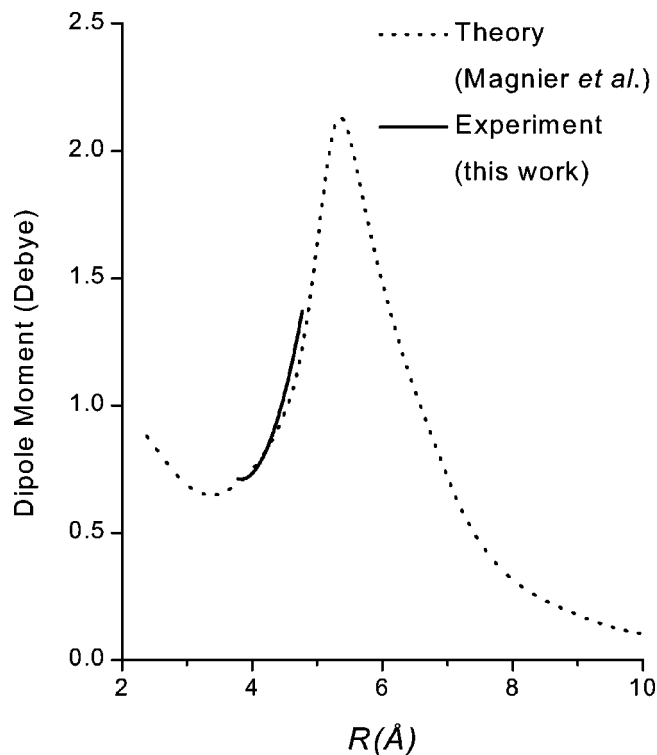
FIG. 8. Comparison of best-fit quadratic $4\,^3\Sigma^+ \rightarrow a(1)\,^3\Sigma^+$ transition dipole moment function $M(R)$ with the calculations of Magnier et al. (Ref. 42).

small wiggles on the inner wall. We plotted the RKR inner wall turning points R_{min} versus energy and fitted these points to the function

$$R_{min} = A_1 \ln[(E - A_2)/A_3], \tag{4}$$

which is equivalent to fitting the energies to an exponential function $E = A_3 \exp(R_{min}/A_1) + A_2$. The inner-wall turning points were corrected to the fitted values, and the outer-wall turning points were also adjusted to maintain the differences $(R_{max} - R_{min})$ calculated in the RKR analysis. We used this smoothed version of the RKR curve as the reference potential $V_0(R)$ in the first iteration of IPA. The standard deviation of the calculated versus experimental energies was 0.74 cm^{-1} for $V_0(R)$.

Following each iteration, we calculated the energy levels of the current IPA potential and compared them with the experimental values. We also plotted the IPA potential to see if any unphysical wiggles had been introduced during that iteration. In the early iterations, we used a very coarse grid of points (starting with $P = 5$) and we slowly increased this number in subsequent iterations (eventually reaching $P = 35$). Using more grid points led to wiggles on the inner or outer wall. The IPA program allows the user to freeze the potential for some grid points while varying it for others in a particular iteration. Therefore, once relatively good agreement was obtained for the lower-level energies, we froze the potential near the bottom of the well and only varied points higher on the inner wall or on the outer wall (or both). The final IPA curve, listed in Table 3 of the accompanying EPAPS file,[52] was obtained by seeking a compromise between the goals of a reasonably smooth curve and good agreement between calculated and measured level energies. The standard deviation of the calculated versus experimental level energies for the final IPA potential is 0.14 cm^{-1}. The IPA potential obtained in this work is shown in comparison to the theoretical potential of Magnier et al.[41,42] in Fig. 7.

D. The $4\,^3\Sigma^+ \rightarrow a(1)\,^3\Sigma^+$ transition dipole moment

The intensity of the bound-free $4\,^3\Sigma^+(v', N', J') \rightarrow a(1)\,^3\Sigma^+$ fluorescence emission within a range $d\lambda$ about λ is given by[50]

$$\frac{dI(\lambda)}{d\lambda} d\lambda = \frac{128\pi^5 c^2 \hbar N_u}{3\lambda^6} \sum_{J''} S_{J'J''}$$

$$\times \left[\int_0^\infty \chi_u^{v'J'}(R) M(R) \chi_1^{E_1,J''}(R) dR \right]^2 d\lambda, \tag{5}$$

where N_u is the number of molecules in the upper state and $S_{J'J''}$ is the Honl–London factor. $\chi_u^{v'J'}(R)$ and $\chi_1^{E_1,J''}(R)$ are, respectively, the wave functions for the upper, bound state of energy E_u and for the lower, continuum state of energy E_1. These wave functions are taken to be real, and $\chi_1^{E_1,J''}(R)$ is energy normalized. $M(R)$ is the transition dipole moment function, and $E_u - E_1 = hc/\lambda$. Equation (5) generally predicts oscillatory spectra for cases like this one where the difference potential is monotonic over the relevant range of internuclear separation. The positions of the nodes contain information on the shapes of the upper- and lower-state potentials, and the relative intensities of the peaks reveal information about $M(R)$.

Figure 4(c) shows a series of simulated spectra obtained using the IPA potential obtained in the present work and assuming that the dipole moment $M(R)$ is a constant. The calculations were performed with the program BCONT (Ref. 53). Note that the lower state $a(1)\,^3\Sigma^+$ has a shallow well at

large internuclear separation, so that the short-wavelength end of the fluorescence band consists of unresolved discrete lines that are not calculated by the simulation program. In the present case, due to the shape of the lower-state potential, the long-wavelength end of the resolved fluorescence is determined primarily by the potentials and transition dipole moment at small R, while the short-wavelength end of the fluorescence spectrum is determined by the potentials and dipole moment at large R. Thus a comparison of the simulations and experimental spectra of Fig. 4(c) indicates that the transition dipole moment function must increase as R increases over the range 3.7–5.5 Å. We have fitted the experimental spectra [relative intensities of the bound-free oscillations in Fig. 4(a)] using a quadratic approximation for the dipole moment function, $M(R) = M_0 + M_1(R - R_e)/R_e + M_2(R - R_e)^2/R_e^2$, where $R_e = 4.20$ Å is the measured equilibrium separation of the $4\,^3\Sigma^+$ state. Since the measurements determine relative intensities, only the ratios M_1/M_0 and M_2/M_0 are determined. The best-fit values obtained were $M_1/M_0 = 2.865$ and $M_2/M_0 = 15.882$. Figure 8 compares our best fit $M(R)$ for the $4\,^3\Sigma^+ \rightarrow a(1)\,^3\Sigma^+$ transition moment with the corresponding theoretical results of Magnier *et al.*[42] In this figure, the experimental dipole moment was scaled to the theoretical function at $R = R_e$. The agreement is quite good over the limited range where comparison is possible. Figure 4(b) shows a comparison of the experimental spectra with simulations carried out using the present IPA potential for the $4\,^3\Sigma^+$ state, the composite experimental $a(1)\,^3\Sigma^+$ potential of Refs. 28 and 54, and the dipole moment function calculated by Magnier *et al.*[42]

E. Analysis of the hyperfine structure

Our interpretation of the $4\,^3\Sigma^+$ hyperfine structure is based on analyzing the angular momentum coupling that is intermediate between Hund's limiting cases $b_{\beta J}$ and $b_{\beta S}$. Our starting point[57–61] is the Hamiltonian

$$\mathbf{H} = \mathbf{H}_{\text{rot}} + A\mathbf{L}\cdot\mathbf{S} + b\mathbf{I}\cdot\mathbf{S} + \gamma\mathbf{N}\cdot\mathbf{S} + \epsilon(3S_z^2 - \mathbf{S}^2), \qquad (6)$$

where $\mathbf{H}_{\text{rot}}$ is the rotational Hamiltonian, $A\mathbf{L}\cdot\mathbf{S}$ is the spin–orbit interaction, $b\mathbf{I}\cdot\mathbf{S}$ is the Fermi contact interaction,[62] which is the dominant contribution to the hyperfine structure of Rydberg states in alkali molecules,[27,40,62,63] and $\epsilon(3S_z^2 - \mathbf{S}^2)$ is the spin–spin term. As usual, $\mathbf{N}$ is the sum of the rotational angular momentum of the nuclei ($\mathbf{R}$) plus the electron orbital angular momentum ($\mathbf{L}$), $\mathbf{S}$ is the total electron spin, and $\mathbf{I}$ is the nuclear spin. We take $\mathbf{I}$ to be the nuclear spin of Na only, since the nuclear magnetic moment of Na is much larger than that of K.

We consider the matrix representation of $\mathbf{H}$ in a Hund's case b basis, modified to include nuclear spin. The case b basis functions may be denoted $|\alpha NSJM_J\rangle$, and they specify the electronic, vibrational, and rotational degrees of freedom: α is shorthand for the $4\,^3\Sigma^+$ electronic state ($\Lambda = 0$) and a particular vibrational level v, and N, S, J, and M_J are the angular momentum quantum numbers. The simplest way to add the nuclear spin is to define direct product states $|\alpha NSJM_J\rangle|IM_I\rangle$. Alternatively, one may use the basis states $|\alpha NSJI;FM_F\rangle$, which correspond to the coupling scheme

$$\mathbf{N} + \mathbf{S} = \mathbf{J}, \quad \mathbf{J} + \mathbf{I} = \mathbf{F}. \qquad (7)$$

The states $|\alpha NSJI;FM_F\rangle$ are eigenfunctions of N, S, J, I, F, and M_F and may be constructed as follows:

$$|\alpha NSJI;FM_F\rangle = \sum_{M_J}\sum_{M_I} C(JM_J, IM_I; FM_F)|\alpha NSJM_J\rangle|IM_I\rangle, \qquad (8)$$

where $C(\cdots)$ is a Clebsch–Gordan coefficient. Using sum rules for the Clebsch–Gordan coefficients,[64] it can be shown that

$$\langle\alpha N'SJ'I;FM_F|\mathbf{H}_{\text{rot}}|\alpha NSJI;FM_F\rangle = \delta_{J'J}\delta_{N'N}\langle\alpha NSJM_J|\mathbf{H}_{\text{rot}}|\alpha NSJM_J\rangle. \qquad (9)$$

The states $|\alpha NSJI;FM_F\rangle$ correspond to Hund's case $b_{\beta J}$ (Ref. 62). In this basis, both $\mathbf{H}_{\text{rot}}$ and $\gamma\mathbf{N}\cdot\mathbf{S}$ are diagonal. Following well-established procedures,[58–60] one can arrive at the following matrix elements:

$$\langle\alpha N'SJ'I;FM_F|(\mathbf{H}_{\text{rot}} + \gamma\mathbf{N}\cdot\mathbf{S})|\alpha NSJI;FM_F\rangle = \delta_{J'J}\delta_{N'N}\{B_v N(N+1) + \tfrac{1}{2}\gamma[J(J+1) - N(N+1) - S(S+1)]\}. \qquad (10)$$

For triplet states $S = 1$, and so for each N, J takes on the values $N-1$, N, and $N+1$. Higher order terms such as $D_v[N(N+1)]^2$ may be added as needed.

The alternative coupling scheme

$$\mathbf{S} + \mathbf{I} = \mathbf{G}, \quad \mathbf{G} + \mathbf{N} = \mathbf{F}, \qquad (11)$$

which is denoted $b_{\beta S}$ (Ref. 62), corresponds to a basis $|\alpha SIGN;FM_F\rangle$ in which the Fermi contact term $b\mathbf{I}\cdot\mathbf{S}$ is diagonal. That is,

$$\langle\alpha SIG'N';FM_F|b\mathbf{I}\cdot\mathbf{S}|\alpha SIGN;FM_F\rangle = \delta_{G'G}\delta_{N'N}\frac{b}{2}[G(G+1) - I(I+1) - S(S+1)], \qquad (12)$$

where G takes on the values $|I-S|,\ldots,|I+S|$. In the present case ($S=1$ and $I=\frac{3}{2}$), $G=\frac{1}{2}$, $\frac{3}{2}$, and $\frac{5}{2}$. The unitary transformation between the two possible basis sets is given by standard angular momentum algebra:[64]

$$\langle\alpha N'SJI;FM_F|\alpha SIGN;FM_F\rangle=\delta_{N'N}(-1)^{F+I+S+N}\sqrt{(2J+1)(2G+1)}\begin{Bmatrix}G & S & I\\ J & F & N\end{Bmatrix},\tag{13}$$

where $\{\cdots\}$ is a $6j$ symbol. Using this transformation between the basis sets, it is straightforward to set up and diagonalize the matrix representation of the Hamiltonian.

For a Σ state in Hund's case b, the spin–orbit term in Eq. (6) can be taken to be zero as long as no second-order perturbations are considered. Also, there is no clear experimental indication that ϵ is different from zero. Therefore, for the calculations we performed on the $4\,^3\Sigma^+$ state, we dropped the spin–orbit term, and we usually set $\epsilon=0$. With these simplifications, the analysis above corresponds to the classic situation where the appropriate coupling scheme depends on the relative values of the coupling constants (γ and b) for two different parts of the Hamiltonian. Since N is a good quantum number in either the $b_{\beta J}$ or the $b_{\beta S}$ basis, the Hamiltonian reduces to

$$\mathbf{H}=B_v N(N+1)+b\mathbf{I}\cdot\mathbf{S}+\gamma\mathbf{N}\cdot\mathbf{S}.\tag{14}$$

This form emphasizes that the Hamiltonian consists of a constant energy depending only on N plus two terms $\mathbf{I}\cdot\mathbf{S}$ and $\mathbf{N}\cdot\mathbf{S}$, which are multiplied by different parameters. This type of situation was nicely analyzed by Condon and Shortley,[65] who showed that the relative energy spacings for any ratio of the two parameters could be written using dimensionless parameters. To exploit the parallel to the situation Condon and Shortley considered, we rewrite $\mathbf{N}\cdot\mathbf{S}$ as $|\mathbf{N}|\hat{\mathbf{N}}\cdot\mathbf{S}$, where $\hat{\mathbf{N}}$ is a unit vector. Now one part of the Hamiltonian obviously scales as $\gamma|\mathbf{N}|\approx\gamma(N+\frac{1}{2})$, and another part as b, leading us to expect that the relative energy level differences should depend primarily on the ratio $(N+\frac{1}{2})\gamma/b$.

We have found, by direct numerical calculation, that this predicted scaling is essentially exact in the limit of large N. Figure 9 illustrates the results obtained. For a particular N, we show reduced energy levels as a function of $\chi=2b/(N$
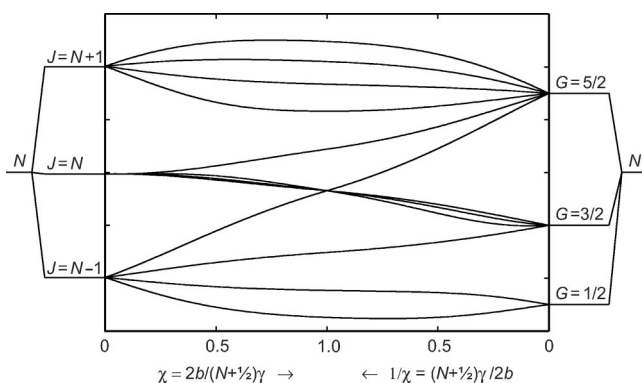

FIG. 9. Correlation diagram showing the transition between Hund's cases $b_{\beta J}$ (on the left) and $b_{\beta S}$ (on the right). The hyperfine energies (scaled as described in the text) are shown as a function of the dimensionless ratio χ $=2b/(N+\frac{1}{2})\gamma$. On the left hand side χ increases from 0 to 1, and on the right $1/\chi$ decreases from 1 to 0.

$+\frac{1}{2})\gamma$. For $N\gtrsim15$, we obtain essentially the same reduced energies for any value of γ/b. The reduced energies were obtained by dividing the absolute energies [obtained by direct diagonalization of Eq. (14)] by $\sqrt{\gamma^2(N+\frac{1}{2})^2+(2b)^2}$ and then adding the same constant to all the energies to make the average zero. The reduced energies are well described as a universal function of χ. In other words, for any specific values of N, γ, and b, the reduced energies will fall very nearly on the universal curve at the point $\chi=2b/(N+\frac{1}{2})\gamma$. We tested this scaling extensively using many values of γ and b, and N in the range 8–100. (Small values of N were omitted because in that case fewer than 12 hyperfine levels exist.) The left-hand side of Fig. 9 corresponds to the limiting case $b_{\beta J}$, for which $(N+\frac{1}{2})\gamma\gg2b$. In this case, the spin-rotation interaction [depending on $(N+\frac{1}{2})\gamma$] leads to the coarse splitting of the states, and the hyperfine interaction (depending on b) causes smaller structure. The right-hand side corresponds to Hund's case $b_{\beta S}$, for which $2b\gg(N+\frac{1}{2})\gamma$. Here the roles of the spin-rotation and hyperfine interactions are reversed. The midpoint of the graph is $\chi=1$ or equal coupling strengths $(N+\frac{1}{2})\gamma=2b$. For the $4\,^3\Sigma^+$ levels we have investigated, the ratio γ/b is such that $1/\chi$ changes from around 0.3 for $N\sim14$ to around 0.9 for $N\sim46$. Therefore, as N increases, one expects to see a transformation in the structure of the hyperfine multiplets that corresponds to moving from the right-hand side of Fig. 9 towards the middle.

The present situation ($\Lambda=0$) is simpler than the general case, because without the spin–orbit interaction there are no matrix elements connecting states of the same J and different N. For a general Λ, we diagonalize a 12×12 matrix for each value of F that includes states with $N=F-\frac{5}{2},F-\frac{3}{2},\ldots,$ $F+\frac{5}{2}$. States of one rotational level N and a given F may be coupled to the states of the same F and a different N. To obtain all the states for a particular N, we must diagonalize matrices for several values of F. The coupling between N and N' levels does not occur for Σ states, so in this case the correlation diagram in Fig. 9 represents all the coupled states for any given N. The only effect of the specific value of N is to set an absolute energy, $B_v N(N+1)$ (plus a term involving D_v if needed). Another simplification in the present discussion is that the spin–spin term is neglected. The simple dependence on $(N+\frac{1}{2})\gamma/b$ no longer holds when ϵ is nonzero.

F. Method of fitting the hyperfine structure

We wish to determine the parameters b and γ for the model Hamiltonian given by Eq. (14) that best fit the data. In principle these parameters may depend on v, and our results will confirm that γ does exhibit a strong dependence on v. We will describe first the techniques we used to fit the hyperfine structure of each (v,N) level separately. The basic

TABLE IV. Results of individual fits that determined b and γ for each (v,N) level indicated. The last column gives the RMS deviation of fitted hyperfine level energies from the measured energies.

v	N	b $(10^{-2}$ cm$^{-1})$	γ $(10^{-4}$ cm$^{-1})$	RMS deviation $(10^{-4}$ cm$^{-1})$
0	39	1.018	1.44	
1[a]	37	1.0	2.0	
2[a]	37	1.0	2.0	
4[a]	39	1.0	2.0	
5[a]	39	1.0	2.0	
6	39	1.013	2.11	0.95
7	39	1.026	2.32	1.94
8	39	1.018	2.22	2.56
9[a]	39	1.0	2.0	
11[a]	39	1.0	2.0	
13	37	0.910	5.79	10.5
13	39	0.879	6.46	15.6
15[a]	39	1.0	2.0	
16	39	1.047	6.98	10.0
17	39	0.930	3.46	
17	37	0.952	3.88	
20	14	0.960	4.72	3.50
23	37	0.974	4.18	
25	25	0.985	3.18	4.16
25	27	0.996	3.33	3.00
28	37	0.997	3.66	6.01
28	39	0.983	3.62	3.40
29	44	1.018	3.73	5.59
29	46	1.030	3.52	6.61
32	16	1.029	4.02	3.53
34	39	1.034	4.14	

[a]For this v, the value of γ given is an estimated upper bound.

FIG. 10. Comparison between experiment and theory for the hyperfine splittings of the indicated (v,N) levels of the $4\,^3\Sigma^+$ state. The horizontal axis is in cm^{-1}, and the displacement of each scan along the vertical axis is proportional to $(N+\frac{1}{2})\gamma$, according to the scaling predicted by theory. The largest peak of each experimental scan is lined up with the average of the three closely spaced theoretical levels. The stick spectra show the spacings predicted by the correlation diagram of Fig. 9. The line in each of the P and R spectra forbidden because of selection rules is omitted.

computational tool is a nonlinear least-squares fitting program based on the Levenberg–Marquardt algorithm.

As discussed in the previous section, we can calculate the energies of the 12 hyperfine levels for a given (v,N) for any specific values of b and γ. Since B_v (as well as D_v and T_v) contributes only an additive constant to the absolute energies [cf. Eq. (14)], we can treat each (v,N) level completely independently if we consider only energy differences between the hyperfine levels. Twelve energies would provide 11 pieces of data to be fitted by two parameters. However, several issues complicate that simple picture. The 12 energy levels for each (v,N) could not always be clearly assigned to peaks in the experimental scans. In some cases, two or more levels were separated by less than their homogeneous linewidths. In other cases, peak positions were difficult to resolve due to low signal-to-noise ratios. Finally, one of the 12 lines is missing from each spectrum because of selection rules.

To account for these complications, we based the fitting procedure on the following two-step strategy. We first identified the peaks whose assignments were reasonably certain. For example, from Fig. 9 it is clear that, near the $b_{\beta S}$ limit $(1/\chi \ll 1$, right-hand side of Fig. 9), the first three energies (counting from the bottom) are usually well separated and that the next three energies are always very close together. We normally took the average of the fourth, fifth, and sixth calculated hyperfine energies to give a single value to fit to the large central peak. The seventh peak (again, assuming the ordering on the right-hand side of the correlation diagram)
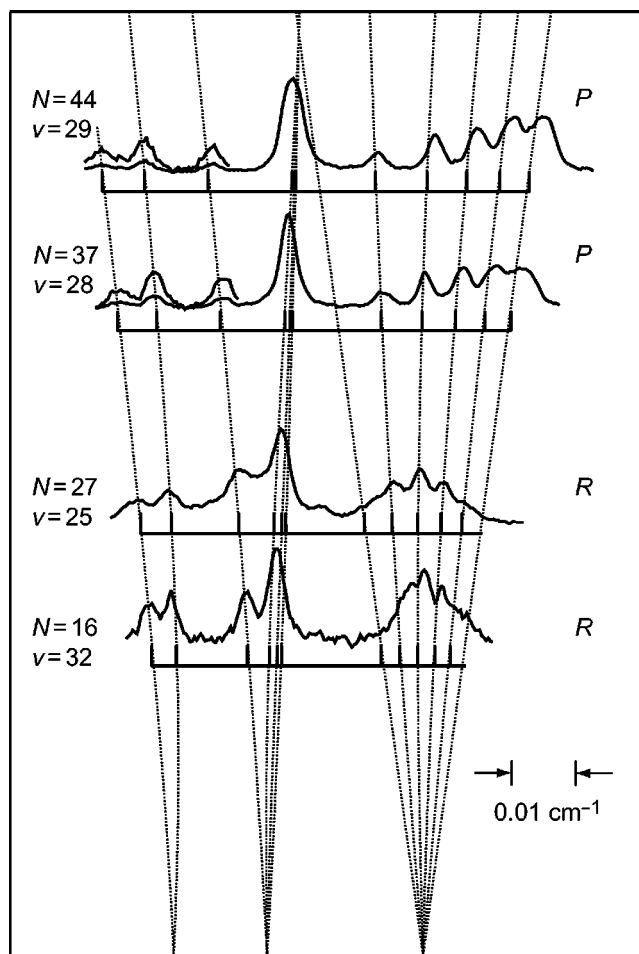
often could also be easily identified. This peak appears in the R branch spectrum shown in Fig. 2(d). We obtained preliminary values of b and γ for each (v,N) level by fitting three to five spacings between the clearly resolved peaks. The results of the preliminary fit predicted positions for all 12 hyperfine energies, and we used those positions to assign the remaining experimental peaks to specific states. The fit was then performed again, including additional energy spacings. The new values for b and γ never changed by more than 5%. Table IV shows the results of these fits. Table IV also reports estimates of b and γ for several additional experimental scans where some peaks were too close to be resolved. All of the results in the table are consistent with the conclusion that b has the value 0.99 ± 0.04 cm^{-1} for these $4\,^3\Sigma^+$ rovibrational levels. This result is within a few percent of values measured for the $1\,^3\Delta$ (Ref. 1) and $c(2)\,^3\Sigma^+$ (Refs. 26, 38, and 40) electronic states of NaK.

Once we have determined values of b and γ for each of the (v,N) levels considered, we can investigate how each scan corresponds to a different point on the correlation dia-

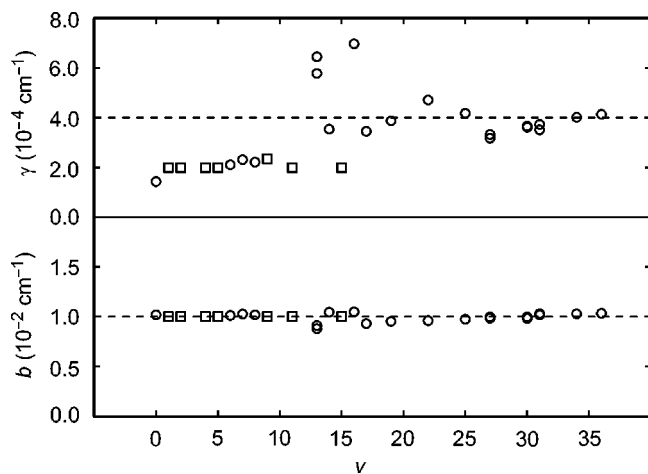FIG. 11. The best-fit values of b and γ as a function of v. The circles indicate best-fit values, and the squares are estimated upper bounds.

gram in Fig. 9. Figure 10 shows selected results that illustrate how the experimental results for different (v,N) levels correspond to different intermediate angular momentum coupling. The dotted lines are theoretical calculations of the absolute energy spacings (horizontal axis) as a function of $(N+\frac{1}{2})\gamma$ (vertical axis) for the fixed value $b = 0.977 \times 10^{-2}$ cm^{-1}, a typical value of b from the individual fits in Table IV.

Another way to consider the results is to examine the dependence of b and γ on v. Figure 11 presents our results in this way; the best-fit values are shown for every (v,N) level considered. The bottom panel shows that the dependence of b on v is quite weak. The most striking feature of the data is that γ exhibits a very strong v dependence. Our preliminary interpretation is that this structure arises because γ is the sum of two terms: $\gamma = \gamma^{(1)} + \gamma^{(2)}$ (Refs. 66–69). Here $\gamma^{(1)}$ arises in first-order perturbation theory as the average value, in the electronic state of interest, of a particular one electron operator. $\gamma^{(2)}$ appears in second-order perturbation theory when the effects of other electronic states are taken into account. We suspect that $\gamma^{(1)}$ depends smoothly on v over the range shown in the figure and that $\gamma^{(2)}$ exhibits a strong dependence on v due to the varying strength of the perturbation by the nearby 3 $^3\Pi$ electronic state.

We also investigated the effect of including a spin–spin interaction [cf. Eq. (6)]. We used the same procedure as before; several (v,N) scans were fitted separately. The parameters adjusted were b, γ, and the spin–spin constant ϵ. The final values of b and γ for each v were within 8% of those determined on the first pass. Most of the values of ϵ fell between -2.4×10^{-3} and -1.5×10^{-3} cm^{-1}, although the value for $(v,N) = (25,27)$ was anomalously low ($\epsilon = -5.4 \times 10^{-4}$ cm^{-1}).

Including the spin–spin interaction leads to slightly better agreement between experiment and theory; the calculated energies come closer to several individual peaks. The values of b in the individual fits show a weak dependence on vibrational number, and the best fit values of γ still exhibit a strong dependence on v. Although we did not perform a full statistical analysis, we do not think including three adjustable parameters instead of two leads to any useful new information. The fit using b and γ appears preferable. The objective of further work will be to develop a quantitative explanation of the v dependence of these parameters.

IV. CONCLUSIONS

We have measured the energies of 107 rovibrational levels of the NaK 4 $^3\Sigma^+$ state using PFOODR spectroscopy. We also measured spectrally resolved 4 $^3\Sigma^+ \to a(1)\,^3\Sigma^+$ bound-free fluorescence, which enabled us to establish the absolute vibrational numbering of the 4 $^3\Sigma^+$ levels. The measured level energies were used to determine the 4 $^3\Sigma^+$ potential with the RKR and IPA methods. The potentials obtained are very similar to the theoretical potential of Magnier et al.[41,42] We also calculated the intensity of the bound-free fluorescence as a function of wavelength, using several transition dipole moment functions $M(R)$. The quality of the RKR and IPA potentials determined in this work is validated by their ability to reproduce the positions of the peaks and troughs of the oscillating spectra. Similarly, the quality of the transition dipole moment function is tested by its ability to reproduce the relative magnitudes of the peaks in the oscillatory spectra. The spectra calculated using the transition dipole moment of Magnier et al. agree very well with the experimental spectra, confirming the high quality of the theoretical calculations. A slightly better fit was obtained by varying $M(R)$ using a quadratic trial function.

The 4 $^3\Sigma^+$ hyperfine structure presents a unique signature pattern resulting from a combination of spin-rotation and Fermi-contact interactions. We have analyzed this structure and determined the Fermi contact constant b and the spin-rotation constant γ for many of the levels. The results indicate that the angular momentum coupling scheme varies with N, shifting from the limiting case $b_{\beta S}$ towards $b_{\beta J}$ as N increases. The Fermi contact constant is independent of vibrational level, while the spin-rotation parameter varies considerably with v. Future work will explore this dependence in more detail.

[1] J. Huennekens, I. Prodan, A. Marks, L. Sibbach, E. Galle, T. Morgus, and Li Li, J. Chem. Phys. **113**, 7384 (2000).
[2] V. S. Ivanov, V. B. Sovkov, Li Li, A. M. Lyyra, G. Lazarov, and J. Huennekens, J. Mol. Spectrosc. **194**, 147 (1999).
[3] H. Katô, M. Sakano, N. Yoshie, M. Baba, and K. Ishikawa, J. Chem. Phys. **93**, 2228 (1990).
[4] Y. Liu, J. Li, H. Gao, D. Chen, Li Li, R. W. Field, and A. M. Lyyra, J. Chem. Phys. **108**, 2269 (1998).
[5] J. Li, Y. Liu, H. Chen, H. Gao, J. Xiang, D. Chen, G. Wu, Li Li, and R. W. Field, J. Chem. Phys. **108**, 7707 (1998).
[6] Li Li and A. M. Lyyra, Spectrochim. Acta, Part A **55**, 2147 (1999).
[7] Li Li and R. W. Field, J. Mol. Spectrosc. **123**, 237 (1987).
[8] Li Li, Q. Zhu, and R. W. Field, J. Mol. Spectrosc. **134**, 50 (1989).

[9] Li Li, Q. Zhu, and R. W. Field, Mol. Phys. **66**, 685 (1989).

[10] T.-J. Whang, A. M. Lyyra, W. C. Stwalley, and Li Li, J. Mol. Spectrosc. **149**, 505 (1991).

[11] T.-J. Whang, W. C. Stwalley, Li Li, and A. M. Lyyra, J. Mol. Spectrosc. **155**, 184 (1992).

[12] G. Lazarov, A. M. Lyyra, Li Li, and J. Huennekens, J. Mol. Spectrosc. **196**, 259 (1999).

[13] X. Xie and R. W. Field, J. Mol. Spectrosc. **117**, 228 (1986).

[14] Li Li, T. An, T.-J. Whang, A. M. Lyyra, W. C. Stwalley, R. W. Field, and R. A. Bernheim, J. Chem. Phys. **96**, 3342 (1992).

[15] Li Li, A. Yiaannopoulou, K. Urbanski, A. M. Lyyra, B. Ji, W. C. Stwalley, and T. An, J. Chem. Phys. **105**, 6192 (1996); **106**, 8626(E) (1997).

[16] D. S. Chen, L. Li, X. T. Wang, Li Li, Q. Hui, H. Ma, L. Q. Li, X. Y. Xu, and D. Y. Chen, J. Mol. Spectrosc. **161**, 7 (1993).

[17] A. Yiannopoulou, B. Ji, Li Li, M. Li, K. Urbanski, A. M. Lyyra, W. C. Stwalley, and G.-H. Jeung, J. Chem. Phys. **101**, 3581 (1994).

[18] C. Linton, F. Martin, A. J. Ross, I. Russier, P. Crozet, A. Yiannopoulou, Li Li, and A. M. Lyyra, J. Mol. Spectrosc. **196**, 20 (1999).

[19] X. Dai, J. O. Clevenger, Y. Liu, M. Song, J. Shang, D. Chen, R. W. Field, and Li Li, J. Mol. Spectrosc. **200**, 120 (2000).

[20] Li Li and R. W. Field, J. Phys. Chem. **87**, 3020 (1983).

[21] B. Ji, C.-C. Tsai, Li Li, T.-J. Whang, A. M. Lyyra, H. Wang, J. T. Bahns, W. C. Stwalley, and R. J. LeRoy, J. Chem. Phys. **103**, 7240 (1995).

[22] Y. Liu, J. Li, M. Xue, D. Chen, Li Li, and G.-H. Jeung, J. Chem. Phys. **103**, 7213 (1995).

[23] J. Li, Y. Liu, H. Gao, M. Xue, D. Chen, and Li Li, J. Mol. Spectrosc. **175**, 13 (1996).

[24] Li Li, A. M. Lyyra, W. T. Luh, and W. C. Stwalley, J. Chem. Phys. **93**, 8452 (1990).

[25] J. T. Kim, H. Wang, C.-C. Tsai, J. T. Bahns, W. C. Stwalley, G. Jong, and A. M. Lyyra, J. Chem. Phys. **102**, 6646 (1995); **103**, 9891(E) (1995).

[26] M. Baba, K. Nishizawa, N. Yoshie, K. Ishikawa, and H. Katô, J. Chem. Phys. **96**, 955 (1992).

[27] K. Ishikawa, J. Chem. Phys. **98**, 1916 (1993).

[28] K. Ishikawa, N. Mukai, and M. Tanimura, J. Chem. Phys. **101**, 876 (1994).

[29] Li Li, X. Dai, Y. Liu, J. O. Clevenger, R. W. Field, G.-H. Jeung, N. Geum, and A. M. Lyyra, J. Mol. Spectrosc. **205**, 139 (2001).

[30] H. Katô, M. Otani, and M. Baba, J. Chem. Phys. **89**, 653 (1988).

[31] W. Yinde, W. Chongye, L. Mingguang, and Li Li, Chin. Phys. Lasers **15**, 359 (1988).

[32] H. Katô, M. Otani, and M. Baba, J. Chem. Phys. **91**, 5124 (1989).

[33] H. R. Xia, L. S. Ma, J. W. Xu, M. Yuan, and I. S. Cheng, Opt. Commun. **76**, 345 (1990).

[34] Y. Liu, B. Ji, A. S.-C. Cheung, W. C. Stwalley, R. W. Field, A. M. Lyyra, and Li Li, J. Chem. Phys. **115**, 3647 (2001).

[35] Li Li, A. Lazoudis, P. Yi, Y. Liu, J. Huennekens, R. W. Field, and A. M. Lyyra, J. Chem. Phys. **116**, 10 704 (2002).

[36] S. Kasahara, T. Ebi, M. Tanimura, H. Ikoma, K. Matsubara, M. Baba, and H. Katô, J. Chem. Phys. **105**, 1341 (1996).

[37] Y.-C. Wang, K. Matsubara, and H. Katô, J. Chem. Phys. **97**, 811 (1992).

[38] P. Kowalczyk, B. Krüger, and F. Engelke, Chem. Phys. Lett. **147**, 301 (1988).

[39] P. Kowalczyk, J. Chem. Phys. **91**, 2779 (1989).

[40] K. Ishikawa, T. Kumauchi, M. Baba, and H. Katô, J. Chem. Phys. **96**, 6423 (1992).

[41] S. Magnier and Ph. Millié, Phys. Rev. A **54**, 204 (1996).

[42] S. Magnier, M. Aubert-Frécon, and Ph. Millié, J. Mol. Spectrosc. **200**, 96 (2000).

[43] A. Pashov, W. Jastrzębski, and P. Kowalczyk, Comput. Phys. Commun. **128**, 622 (2000).

[44] C. R. Vidal and J. Cooper, J. Appl. Phys. **40**, 3370 (1969).

[45] A. N. Nesmeyanov, *Vapor Pressure of the Elements* (Academic, New York, 1963).

[46] H. Sun, Ph.D. thesis, Lehigh University, 1992.

[47] R. Stair, W. E. Schneider, and J. K. Jackson, Appl. Opt. **2**, 1151 (1963).

[48] S. Gerstenkorn and P. Luc, *Atlas du Spectre D'Absorption de la Molécule D'Iode* (Centre National de la Recherche Scientifique, Paris, 1978).

[49] L. Sibbach-Morgus, P. Burns, A. Marks, I. Prodan, A. P. Hickman, and J. Huennekens (unpublished).

[50] M. Masters, J. Huennekens, W. T. Luh, Li Li, A. M. Lyyra, K. Sando, V. Zafiropulos, and W. C. Stwalley, J. Chem. Phys. **92**, 5801 (1990).

[51] H. Sun and J. Huennekens, J. Chem. Phys. **97**, 4714 (1992).

[52] See EPAPS Document No. E-JCPSA6-119-002331 for tables of rovibrational energy levels and transition frequencies, RKR turning points, and IPA potential curves. A direct link to this document may be found in the online article's HTML reference section. The document may also be reached via the EPAPS homepage (http://www.aip.org/pubservs/epaps.html) or from ftp.aip.org in the directory /epaps/. See the EPAPS homepage for more information.

[53] R. J. LeRoy and G. T. Kraemer, BCONT 2.1: A Computer Program for Calculating Bound→Continuum Transition Intensities for Diatomic Molecules, Chemical Physics Research Report No. CP-650R, University of Waterloo, 2002.

[54] R. Ferber, E. A. Pazyuk, A. V. Stolyarov, A. Zaitsevskii, P. Kowalczyk, H. Chen, H. Wang, and W. C. Stwalley, J. Chem. Phys. **112**, 5740 (2000).

[55] R. J. LeRoy, RKR1: A Computer Program Implementing the First-Order RKR Method for Determining Diatom Potential Energy Curves from Spectroscopic Constants, Chemical Physics Research Report No. CP-425, University of Waterloo, 1992.

[56] R. J. LeRoy, LEVEL 7.5: A Computer Program for Solving the Radial Schrödinger Equation for Bound and Quasibound Levels, Chemical Physics Research Report No. CP-655, University of Waterloo, 2002.

[57] I. Kovács, *Rotational Structure in the Spectra of Diatomic Molecules* (Elsevier, New York, 1969).

[58] J. M. Brown, E. A. Colbourn, J. K. G. Watson, and F. D. Wayne, J. Mol. Spectrosc. **74**, 294 (1979).

[59] R. N. Zare, A. L. Schmeltekopf, W. J. Harrop, and D. L. Albritton, J. Mol. Spectrosc. **46**, 37 (1973).

[60] R. N. Zare, *Angular Momentum* (Wiley, New York, 1988).

[61] D. L. Huestis, in *Atomic, Molecular, and Optical Physics Handbook*, edited by G. W. F. Drake (AIP, New York, 1996).

[62] C. H. Townes and A. L. Schawlow, *Microwave Spectroscopy* (McGraw-Hill, New York, 1955).

[63] H. Katô, Bull. Chem. Soc. Jpn. **66**, 3203 (1993).

[64] A. Messiah, *Quantum Mechanics* (Wiley, New York, 1966), Vol. II.

[65] E. U. Condon and G. H. Shortley, *The Theory of Atomic Spectra* (Cambridge University Press, Cambridge, England, 1991).

[66] T. Bergeman and R. N. Zare, J. Chem. Phys. **61**, 4500 (1974).

[67] J. M. Brown and J. K. G. Watson, J. Mol. Spectrosc. **65**, 65 (1977).

[68] S. Green and R. N. Zare, J. Mol. Spectrosc. **64**, 217 (1977).

[69] H. Lefebvre-Brion and R. W. Field, *Perturbations in the Spectra of Diatomic Molecules* (Academic, Orlando, FL, 1986).